



OPEN

Lessons from time-dependent deflection in record span prestressed concrete bridges

Teng Tong^{1,2}, Chenyi Zhao², Shiyu Wu^{1,3✉}, Jiateng Li² & Zhao Liu^{1,2}

Globally, over 60% of record-span segmentally constructed prestressed concrete (PC) bridges exhibit excessive deflection, severe cracking, and underestimated prestressing losses. Decades of practice in continuous girder and rigid-frame PC bridge design have limited the maximum span capacity to about 350 m, mainly due to unreliable design methodologies and software constraints. This study proposes a multi-field time-dependent numerical framework integrating concrete cracking, nonlinear creep, shrinkage, reinforcement behavior, and prestressing tendon relaxation (including threaded bars). Implemented in Abaqus/Standard through user-defined subroutines, the framework enables high-fidelity 3D simulations and is validated on three record-span PC bridges. Results show that nonlinear creep and cracking significantly aggravate deflection, a phenomenon poorly documented in prior studies. The analysis further reveals that downward-curved cantilever tendons are necessary to counter the unreliable prestressing effectiveness of threaded bars. An in-depth evaluation of these bridges highlights that achieving a reasonable finished stress state is essential for controlling long-term deflection. The findings provide valuable insights for improving the design and durability of segmentally constructed PC bridges.

Keywords Multi-field, Cracking, Nonlinear creep, Record-span PC bridge, Deflection

Recent advances in construction technology have facilitated the widespread implementation of large-span prestressed concrete (PC) structures worldwide^{1–3}. However, these structures are susceptible to time-dependent increases in mid-span deflection caused by concrete shrinkage and creep^{4–7}, prestress loss in tendons^{8–11} and crack coupled effects^{12–14}. Notably, this time-dependent deformation progressively reduces structural performance and, in critical scenarios, may trigger complete structural collapse^{15–17}. Some PC bridges that suffer from excessive, unexpected deflection are listed in Table 1. Obviously, this is a common problem for large-span PC bridges. Consequently, accurate prediction of long-term deflection behaviour and reliable assessment of deterioration performance are therefore critical for implementing appropriate maintenance and retrofitting strategies for such structures^{18,19}.

Finite Element (FE) modelling has emerged as one of the most sophisticated physics-based analytical tools for structural performance evaluation, enabling engineers to gain in-depth understanding of structural behaviour mechanisms. The past decades have witnessed extensive research efforts to significantly improve the reliability of FE modelling results. To name a few, Rincón et al.²³ assessed the deflection of a bridge which is built by the cantilever construction method, considering the time-dependent behaviour of concrete such as creep and shrinkage. Han et al.²⁴ calculated the long-term deflection of a PC bridge based on Chinese code. However, the calculation method of the creep coefficient given in the code does not consider the nonlinear creep effect²⁵. While 3D finite element models can precisely capture shear lag effects, Euler–Bernoulli beam theory may underestimate box girder long-term deformations by approximately 20%^{5,6}. The long-term behaviour of prestressed girders exhibits notable sensitivity to finite element type, particularly in deflection magnitude and time-dependent trends²⁶. While comparative studies between FE simulations and actual field monitoring data are still limited in number, the existing cases provide significant contributions to advancing this research domain.

However, accurate prediction of long-term performance remains a significant challenge for PC box girders. Accurate prediction is challenging due to interdependent time-dependent phenomena including concrete creep, shrinkage, prestress loss of tendons, and material degradation, all interacting through complex physical

¹Key Laboratory of Concrete and Prestressed Concrete Structures of Ministry of Education, School of Civil Engineering, Southeast University, Nanjing 211189, People's Republic of China. ²School of Civil Engineering, Southeast University, Nanjing, Nanjing 211189, People's Republic of China. ³Department of Civil and Environmental Engineering, Politecnico Di Milano, Piazza Leonardo da Vinci N.32, 20133 Milano, Italy. ✉email: 230219153@seu.edu.cn

No	Bridge	Span arrangement (Unit: m)	Service time (Unit: year)	Deflection (Unit: cm)	Deflection and span ratio	Reference
1	KB bridge	72.2 + 241 + 72.2	18	161	0.668%	Bažant et al. ¹⁵
2	Humen auxiliary channel bridge	150 + 270 + 150	8	26	0.096%	Tong et al. ²⁰
3	Jiagnjin bridge	140 + 240 + 140	10	33	0.138%	Huang et al. ¹
4	Lancang bridge	130 + 200 + 80	11	23.6	0.118%	Li et al. ²¹
5	Tianjin bridge	48 + 3 × 64 + 48	5	7.7	0.120%	Meng et al. ²²

Table 1. Cases of excessive deflection bridge.

couplings. Despite all this, many scholars are still trying to consider different physical processes in large-span structures simulation. For instance, Yu et al.²⁷ analysed the excessive deflection of the KB Bridge in Palau using a Kelvin chain model, converting the integral-type creep law into a rate-type formulation. Similarly, Huang et al.¹ developed a three-dimensional FE model incorporating concrete creep, shrinkage, and prestress loss to study deflection and crack development in a three-span prestressed concrete (PC) bridge. Di Luzio et al.³ developed a rate-dependent computational algorithm utilizing continuous retardation spectrum theory, which was incorporated into a 3D finite element framework to analyse time-dependent deformation behaviour of a PC bridge in Romania. More recently, Wu et al.¹⁴ evaluated the deflection of a cantilever-constructed bridge, accounting for time-dependent effects such as creep, shrinkage and concrete damage, they captured the complex interplay between concrete cracking and vertical deflection.

Previous research on PC bridges has frequently relied on individual case studies, limiting the generalizability of their findings. For instance, existing research has primarily applied a single time-dependent numerical model to analyse only one actual bridge^{27,28}. While such studies provide valuable insights into specific structural behaviours, their conclusions may not be readily applicable to other bridges with differing design parameters, loading conditions, or environmental exposures³⁰. To address this gap, this research proposed a multi-field model establishes its broad applicability through a unified theoretical framework that integrates key multi physical processes governing long-term structural behaviour. Its core contribution lies in the concurrent coupling of a viscoelastic model for concrete with a continuum damage mechanics formulation, explicitly capturing the mutual interaction between time-dependent deformation and progressive microcracking. Furthermore, the formulation incorporates a time-dependent algorithm for prestress relaxation loss. A nonlinear creep constitutive relation is introduced to address the elevated stress regimes commonly encountered in critical regions, such as those near anchorages or under sustained high service loads. By resolving the interdependencies among material aging, damage accumulation, and prestress evolution within a single numerical scheme, this integrated approach provides a more rigorous and mechanically consistent prediction of long-term performance in PC bridge structures.

This study systematically develops a comprehensive multi-physics constitutive framework for time-dependent analysis of prestressed concrete bridges, with detailed theoretical derivations and model formulations presented in Section "Multi-field time-dependent numerical model". The computational efficacy and predictive accuracy of the proposed model are validated through three representative case studies of record-span bridges in Section "Case bridge studies". Section "Discussions" provides the discussion on critical factors affecting long-term structural performance, including reasonable stress state, nonlinear creep concrete effects, and prestress loss evolution, etc. Finally, based on numerical findings and mechanistic analysis, some practical design recommendations and construction strategies for future record-span PC bridge projects, aiming to enhance their long-term serviceability and durability.

Multi-field time-dependent numerical model

This section presents the constitutive framework for simulating long-term behaviour of PC bridge. Three interconnected components are established: a concrete model incorporating creep-shrinkage-cracking mechanisms through aging CDP and rate-type formulations (Section "Creep-shrinkage-cracking" model for concrete), a novel prestress relaxation model based on current stress-strain state (Section "Rebar"), and a smeared rebar approach for ordinary reinforcement (Section "Relaxation of Prestressing tendon / Screw-thread rebar"). Their implementation via Abaqus subroutines is detailed in Section "Abaqus/Standard implementation", forming a unified system for analysing time-dependent behaviour.

"Creep-shrinkage-cracking" model for concrete

Concrete behaviour modelling assumes strains can be decomposed additively³¹ as shown in Eq. (1), where the total strain tensor (ϵ) is expressed as the sum of multiple components. These include: (1) the elastic strain (ϵ_e), which is recoverable and occurs instantaneously upon loading; (2) the plastic strain (ϵ_p), representing irreversible deformation; (3) the time-dependent creep strain (ϵ_v); and (4) the shrinkage strain (ϵ_{sh}), which develops due to moisture loss and other environmental factors.

$$\epsilon = \epsilon_e + \epsilon_p + \epsilon_v + \epsilon_{sh} \quad (1)$$

This strain superposition principle is mathematically represented through the uniaxial rheological model illustrated in Fig. 1.

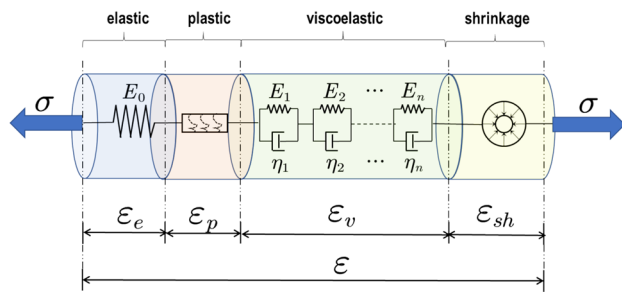


Fig. 1. 1-D rheological illustration of strain additivity assumption.

Mesh-insensitive aging CDP model

The Concrete Damage Plasticity (CDP) model is extensively utilized as one of the most prominent frameworks among various constitutive models for concrete³². As a smeared-crack continuum approach, the CDP model effectively captures two fundamental failure mechanisms: compressive crushing and tensile cracking^{33,34}.

Following foundational work conducted by Hillerborg et al.³⁵ on fracture energy regularization, the mesh-sensitivity characteristic of local constitutive formulations is systematically addressed in this model. Notably, for modelling tensile fracture behaviour, the CDP model employs a stress-crack opening displacement relationship instead of the conventional stress-strain formulation.

The Cauchy stress tensor $\sigma(\varepsilon)$ considering concrete damage can be calculated as:

$$\sigma(\varepsilon) = (1 - d(\kappa)) \mathbb{C} : \varepsilon \quad (2)$$

where ε is the effective strain tensor without plastic strain tensor component; \mathbb{C} is the elastic stiffness tensor of material; κ denotes the maximum equivalent strain experienced during the complete loading history; and $d(\kappa)$ is the scalar damage level which is calculated as follows:

$$d(\kappa) = 1 - \frac{\kappa_0}{\kappa} [1 - \alpha + \alpha \cdot \exp(-\beta(\kappa - \kappa_0))] \quad (3)$$

where κ_0 is the strain corresponding to the peak tensile stress. To address the inherent mesh-sensitivity limitation of conventional local damage formulations, the computational framework incorporates β to regularize fracture energy as follow:

$$\beta = \frac{E \kappa_0 h_e}{G_f} \quad (4)$$

where E is Young's modulus of concrete; G_f is the fracture energy per unit length and h_e represents element characteristic length.

Additionally, the concrete fracture energy G_f is calculated as^{36,37}:

$$G_f = \alpha_a \left(\frac{f'_c}{0.051} \right)^{0.46} \left(1 + \frac{d_a}{11.27} \right)^{0.22} \left(\frac{w}{c} \right)^{-0.30} \quad (5)$$

where d_a is maximum aggregate size in mm; w/c is the water to cement ratio by weight; and α_a is a factor based on the type of aggregate.

The tension softening behaviour (Fig. 2a) of normal-strength concrete is characterized by an exponential stress-cracking displacement expression as³⁸:

$$\frac{\sigma_t}{f_t} = \left[1 + \left(c_1 \frac{\omega_t}{\omega_{cr}} \right)^3 \right] \exp \left(-c_2 \frac{\omega_t}{\omega_{cr}} \right) - \frac{\omega_t}{\omega_{cr}} (1 + c_1^3) \exp(-c_2) \quad (6)$$

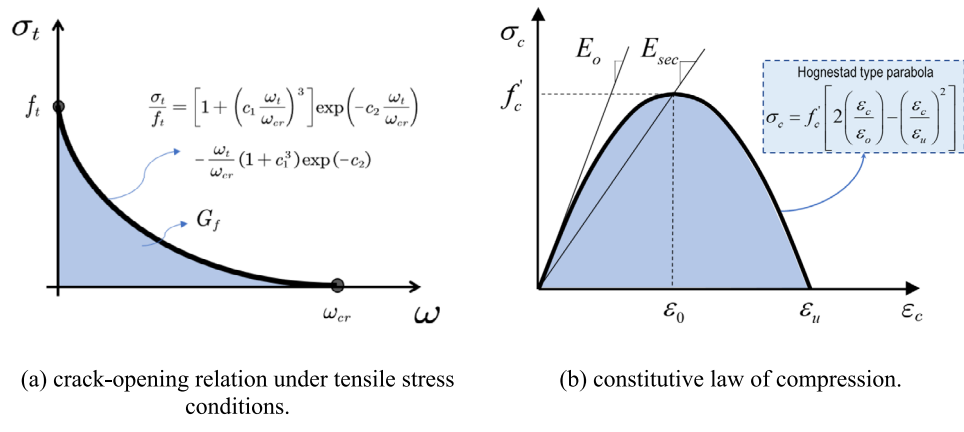
where c_1 and c_2 are constant factors with values of 3.0 and 6.93, respectively; ω_t represents the crack opening displacement; and the crack opening displacement at the complete release of fracture energy can be calculated

as $\omega_{cr} = 5.14 G_f / f_t$.

Compressive damage factor is determined through compressive strain as:

$$d_c = \begin{cases} 1 - \frac{\rho_c n}{n-1+\chi^n} & \chi \leq 1 \\ 1 - \frac{\rho_c}{\alpha_c (\chi-1)^2 + \chi} & \chi > 1 \end{cases} \quad (7)$$

where α_c is a parameter characterizing the post-peak softening behaviour of the envelope curve, the compression constitutive law is shown in Fig. 2b; other parameters are defined as:

**Fig. 2.** CDP model and their regularization form used for concrete.

$$\rho_c = \frac{f_{c,r}}{E_c \varepsilon_{c,r}} \dots n = \frac{E_c \varepsilon_{c,r}}{E_c \varepsilon_{c,r} - f_{c,r}} \dots \chi = \frac{\varepsilon_c}{\varepsilon_{c,r}} \quad (8)$$

where $f_{c,r}$ represents the characteristic compressive strength; ε_c and $\varepsilon_{c,r}$ represent the uniaxial compressive strain and peak compressive strain at $f_{c,r}$, respectively; and E_c is the Young's modulus of the concrete. Relevant details for damage factors can refer to Tong et al.³⁹ and they are not presented for brevity. For a PC bridge, the compressive stress level ranges from 0.3 f_c to 0.6 f_c . Thus, mesh-sensitivity for compression is not as severity as tension.

Nonlinear anisotropic creep model

The rate-type creep formulation proposed by Yu et al.²⁷ offers distinct advantages over the traditional Volterra integral approach. While conventional techniques depend on retaining full stress history to evaluate creep increments, this improved formulation eliminates such requirements and seamlessly integrates with step-by-step FE analysis.

As illustrated in Fig. 1, the model employs a Kelvin chain comprising approximately ten elements. The elastic moduli values of the i -th Kelvin chain unit is defined by the discrete spectrum of the creep compliance function and retardation time τ_i ($i = 1, 2, \dots, n$) as follows:

$$D_i = \frac{1}{L(\tau_i) \ln 10 (1 - \lambda_i)} \quad (9)$$

Where λ_i and β_i are parameters according to retardation time which can be calculated as:

$$\begin{aligned} \lambda_i &= \tau_i (1 - \beta_i) / \Delta t \\ \beta_i &= \exp(-\Delta t / \tau_i) \end{aligned} \quad (10)$$

The discrete spectrum $L(\tau_i)$ in (9) is obtained from the creep compliance function as:

$$L(\tau_i) = -\frac{(-3\tau_i)^3 C'''(3\tau_i)}{(3-1)!} \quad (11)$$

where $C'''(3\tau_i)$ is the third-order derivative of the creep part $C(t, t_{n-1/2})$ which is expressed as:

$$C(t, t_{n-1/2}) = J(t, t_{n-1/2}) - 1/E(t_{n-1/2}) \quad (12)$$

where $J(t, t_{n-1/2})$ is the compliance function of the B4 creep model⁴⁰, $E(t_{n-1/2})$ is the instantaneous elastic modulus at the middle current time step $t_{n-1/2}$. Relevant rate-type formulation implementation is detailed in reference¹⁴.

Finally, the internal variables used in the calculation of creep strain increments are obtained as:

$$\gamma_i^n = \lambda_i \Delta \sigma \frac{1}{D_i} + \beta_i \gamma_i^{n-1} \quad (13)$$

where γ_i^{n-1} is the last time step internal variable. It is noted that the exponential algorithm above ensures unconditional stability when numerically solving first-order ordinary differential equations, thus, the creep strain increment $\Delta \varepsilon_{cr}$ at the current time step is given as the rate type creep form:

$$\Delta \varepsilon_{cr} = \Delta \varepsilon_{cr,1}\mathbf{n}_1 + \Delta \varepsilon_{cr,2}\mathbf{n}_2 + \Delta \varepsilon_{cr,3}\mathbf{n}_3 \quad (14)$$

with.

$$\Delta \varepsilon_{cr,k} = h(\sigma_k) \sum_{i=1}^N (1 - \beta_i) \gamma_i^{n-1} \text{ with } k = 1, 2, \text{ or } 3 \quad (15)$$

where $\mathbf{n}_k (k = 1, 2, 3)$ is eigenvector which are associated with the principal stress $\sigma_k (k = 1, 2, 3)$; and $h(\sigma_k)$ is the nonlinear creep coefficient that determined by stress level as⁴¹:

$$h(\sigma_k) = 1 + \left[2.2 \left(\max \left[\left| \frac{\sigma_k}{f_{c,k}} \right| - 0.3, 0 \right] \right) \right]^{2.5} \dots \text{ with } k = 1, 2, \text{ or } 3 \quad (16)$$

It should be noted that the nonlinear creep coefficient is defined as 1.0 for a stress level $\sigma_k / f_{c,k} \leq 0.3$, wherein creep is considered linear, and is governed by the expression above only when the stress level $\sigma_k / f_{c,k} > 0.3$.

Shrinkage

In this study, the shrinkage strain is defined as the eigenstrain that is not influenced by the level of external stress. In the B4 model, the drying shrinkage strain $\varepsilon_{sh,dry} (t, t_0)$ is evaluated as⁴⁰:

$$\varepsilon_{sh,dry} (t, t_0) = -\varepsilon_{sh,dry\infty} (t_0) k_h S(t, t_0) \quad (17)$$

where $\varepsilon_{sh,dry\infty} (t_0)$ describes the asymptotic shrinkage value as a function of curing age t_0 ; k_h is a factor based on the environmental humidity; and $S(t, t_0)$ is the temporal evolution of shrinkage deformation exhibiting proper asymptotic characteristics can be expressed as⁴²:

$$S(t, t_0) = \tanh \sqrt{t/\tau_{sh}} \quad (18)$$

where the shrinkage halftime τ_{sh} characterizes the drying shrinkage rate, following diffusion-based drying mechanics.

The B4 model also takes into account autogenous shrinkage, which can be calculated by the following formula:

$$\varepsilon_{sh} (t, t_0) = -\varepsilon_{sh,au\infty} [1 + (\tau_{au} / (t + t_0))^\alpha]^{r_t} \quad (19)$$

where r_t is a parameter according to cement type; τ_{au} and α are factors which can be calculated based on water to cement ratio, relevant formula can refer to Wendner et al.⁴⁰.

Rebar

The explicit finite element modelling of all reinforcement bars in PC bridges is computationally prohibitive due to the enormous quantity of rebars involved. Consequently, a smeared reinforcement approach is adopted where the rebars are homogenized within the concrete material, as depicted in Fig. 8a. This implies that the stresses of 1-D rebars are transferred into the stresses inside the concrete element σ_s , as:

$$\sigma_s = \begin{bmatrix} \rho_{s,x} \sigma_{s,x} & & & \mathbf{0} \\ & \rho_{s,y} \sigma_{s,x} & & \\ & & \rho_{s,z} \sigma_{s,z} & \\ \mathbf{0} & & & \mathbf{0} \end{bmatrix} \quad (20)$$

where $\rho_{s,x}$, $\rho_{s,y}$, and $\rho_{s,z}$ are reinforcement ratio along x , y and z directions respectively; $\sigma_{s,x}$, $\sigma_{s,y}$ and $\sigma_{s,z}$ are related to the strains $\varepsilon_{s,x}$, $\varepsilon_{s,y}$ and $\varepsilon_{s,z}$ independently, following the elastic-perfectly plastic material formulation⁴³ as shown in Fig. 3.

Relaxation of prestressing tendon / Screw-thread rebar

Both prestressing tendons and screw-thread rebars are explicitly modelled as embedded elements within the surrounding concrete matrix. The stress relaxation behaviour of prestressing tendons is simulated according to the CEB-FIP model⁴⁴, expressed as:

$$\rho(t) = \rho_{1000} \left(\frac{24 \cdot t}{1000} \right)^\kappa \quad (21)$$

where t is time in day; ρ_{1000} is the relaxation loss after 1000 h at initial stress for different types of prestressed rebar as listed in Table 2, and the corresponding relaxation development is shown in Fig. 4; κ is a coefficient which describes the evolution of relaxation losses over time ($\kappa = 0.16$ in this research).

However, after the prestressed steel bars are tensioned and anchored, the effective prestress in the vertical prestressed rebars is far from the design requirements. On-site test results indicate that the vertical prestress loss exceeds the design value^{45–47}. Thus, the relaxation development of vertical prestressed rebars can be given by:

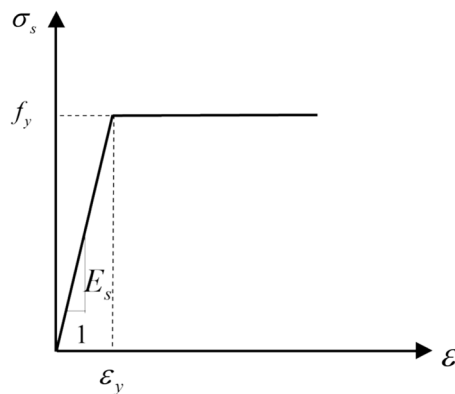


Fig. 3. Constitutive relationship of steel rebars.

Type of prestressed steel	Wires and strands	Rebar diameter ≤ 15mm	Rebar diameter > 15mm
$\sigma_{pi} = 0.7f_p$	2.5%	6.0%	4.0%
$\sigma_{pi} = 0.8f_p$	4.5%	/	/

Table 2. Relaxation loss for different type of prestressed steels. Notes: with initial stress less than 0.5 f_p , the relaxation loss is not considered.

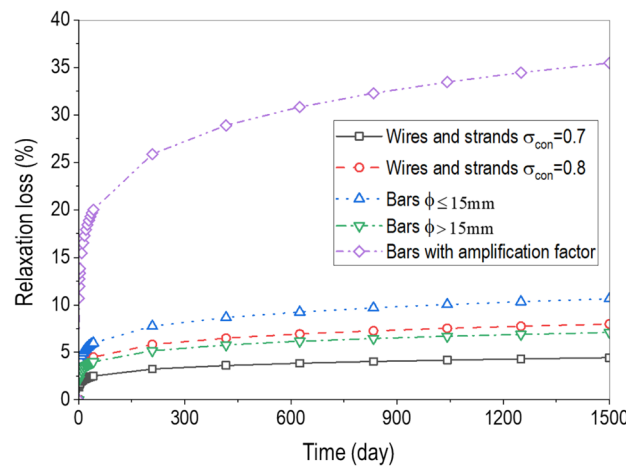


Fig. 4. Relaxation loss of different type prestressing tendons and bars.

$$\rho(t) = C\rho_{1000} \left(\frac{24 \cdot t}{1000} \right)^\kappa \quad (22)$$

$$C = P_e/P_i \quad (23)$$

where P_i and P_e represent the average stress level after prestress loss stabilization and the instantaneous loss immediately after tensioning in the vertical prestressing rebars, respectively. Han et al.²⁴ reported an average prestress loss of 29% in a long-span PC bridge after 20 years of service, with losses in the horizontal and vertical directions reaching 45.4% and 68.6%, respectively. Compared to the standard 1000-h relaxation loss of 2.5%, these significant in-service losses justify the use of a coefficient ($C=10$ in this study) to better reflect real long-term prestress reduction.

Abaqus/Standard implementation

The analysis of long-term structural behaviour is inherently complex due to the intricate interaction of multiple time-dependent phenomena, including concrete damage evolution, creep (both linear and nonlinear), shrinkage, and prestress relaxation. To systematically address these challenges, this study implements an enhanced

computational framework within Abaqus/Standard through the strategic use of specialized user subroutines, as illustrated in Fig. 5.

The framework employs key subroutines to model time-dependent effects. USDFLD manages field variables including concrete age through *FIELD* (1) to control elastic modulus evolution in the CDP model, while UMAT handles reinforcement behaviour. For strain computation, UEXPAN processes increments from creep, shrinkage, and strand relaxation using stress data obtained via GETVRM. The initial stress of the prestressing tendons is introduced via SIGINI, thereby completing the integrated modelling approach. A rate-type constitutive algorithm efficiently computes creep strains, with all strain components stored in STATEV for data consistency. This approach extends the CDP model by incorporating concrete aging while maintaining efficiency via smeared reinforcement representation, enabling robust long-term structural simulations.

To simplify the modelling of reinforced concrete structures, a dummy solid element technique is applied. In this method, two C3D8 hexahedral element layers with distinct identifiers are assigned identical nodal coordinates, as shown in the “Rebar” section of Fig. 6. The concrete layer, identified by element label 1 and comprising nodes 1 to 8, is modelled using the CDP material model with eight Gauss integration points. The reinforcement layer, identified by element label 101 and also comprising nodes 1 to 8, uses the same C3D8 element formulation but is assigned an elastic-perfectly plastic material model for steel. This layer implements a smeared reinforcement approach based on predefined reinforcement ratios in the longitudinal, transverse, and vertical directions. Prestressing strands are modelled separately using T3D2 elements, which are assigned linear elastic material properties.

Case bridge studies

Three well-known record-span PC bridges are selected to verify the proposed numerical model. The authors participated in the relevant analytical work and possess first-hand information on bridge design and inspection. The main spans of the three bridges are 270 m, 245 m, and 268 m, respectively. The geometric details are provided in Table 3.

The traffic load consists of a uniformly distributed load of 10.5 kN/m and a concentrated load of 360 kN, as specified in JTG⁵⁰. In addition, thermal loads, including uniform temperature effects and temperature gradients, are considered according to JTG⁵⁰ provisions. For these bridges located in warm regions, the design temperature extremes are defined as 39 °C for the maximum and -6 °C for the minimum. Temperature 1 at the deck surface is set at 20 °C, while Temperature 2 at mid-depth is assigned 6.7 °C for the temperature gradient analysis. The negative temperature gradient is calculated by multiplying the positive gradient values by a factor of -0.5. All loads are combined using a load factor of 1.0.

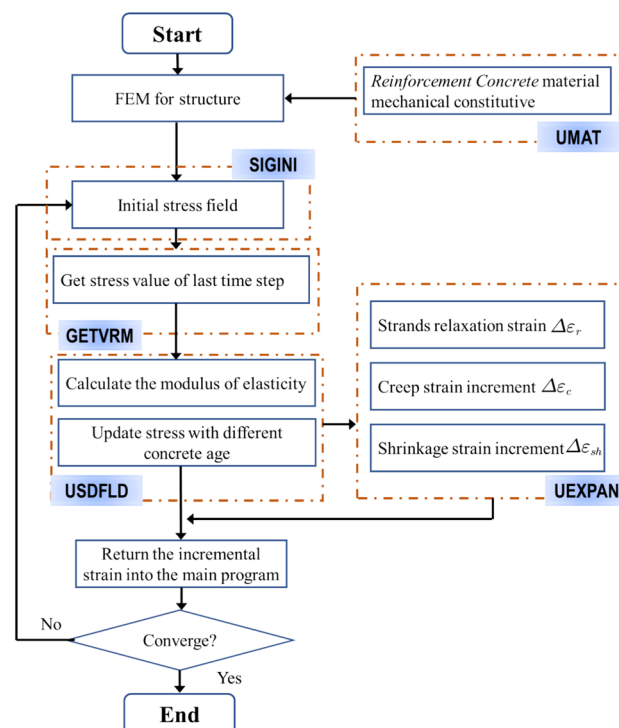


Fig. 5. Abaqus/Standard implementation flowchart.

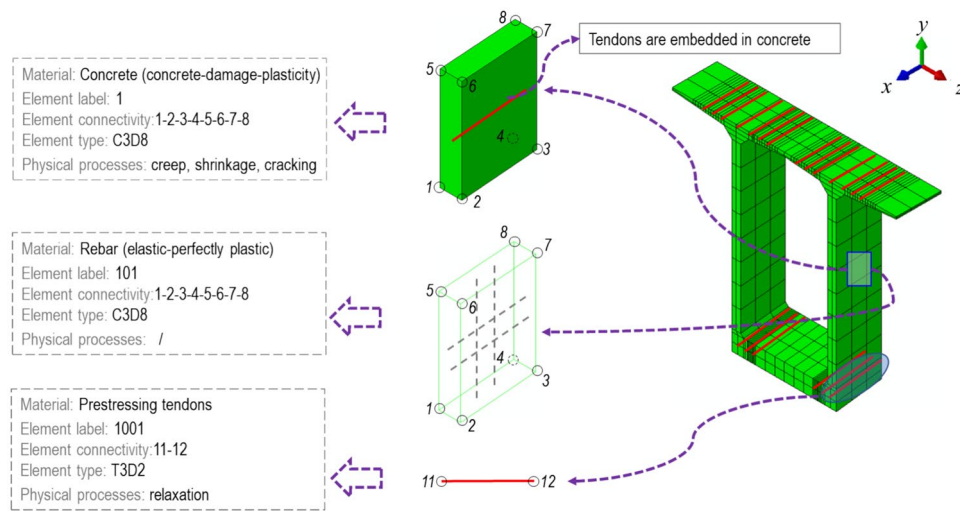


Fig. 6. Fundamental elements in the simulation framework.

No	Span arrangement (Unit: m)	Concrete	Height/Span	Web thickness (Unit: m)	Bottom slab thickness (Unit: m)
Bridge I	150 + 270 + 150	C50	1/18.24	0.4 ~ 0.6	0.32 ~ 1.30
Bridge II	162.5 + 3 × 245 + 162.5	C50	1/18.85	0.5 ~ 0.8	0.32 ~ 1.35
Bridge III	140 + 268 + 140	C60	1/17.87	0.45 ~ 1.0	0.32 ~ 1.70

Table 3. Geometries details of three case bridges.

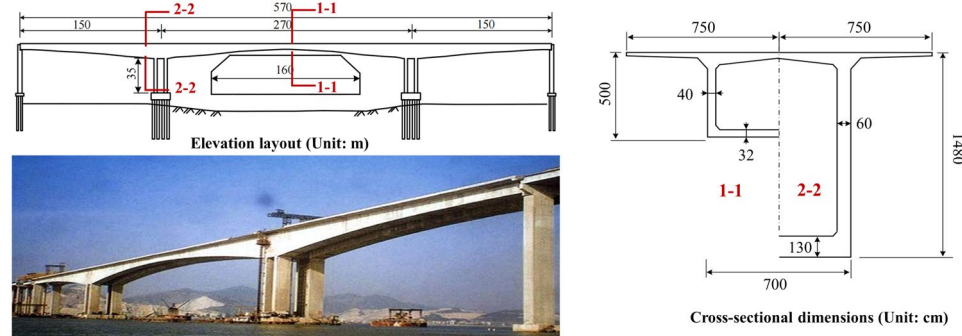


Fig. 7. Elevation layout and cross-sectional dimensions of bridge I.

Bridge I: a three span (150 + 270 + 150) PC bridge

Bridge details

The Bridge I is a continuous three-span prestressed concrete rigid-frame structure with a box girder configuration, arranged in spans of 150 m + 270 m + 150 m. Detailed dimensions of the main pier and the mid-span cross-section are shown in Fig. 7. The girder depth varies parabolically along the span, measuring 5.0 m at mid-span and increasing to 14.8 m at the piers. Segmental construction was adopted using the balanced cantilever method, with the main span consisting of 63 segments and each side span comprising 36 segments. Longitudinal prestress was applied through 66 tendon groups within the top slab and 28 within the bottom slab, while vertical prestressing was introduced via 32 mm diameter screw-thread placed inside the webs at 1 m spacing to enhance shear resistance. The mix design parameters of the box girder concrete are as follows: water-cement ratio (0.38), sand ratio (0.42), slump (18 cm), density (2450 kg/m³), and 28-day mean cylindrical compressive strength (34.3 MPa).

The structural deflection monitoring work was launched 180 days after the bridge opened to traffic. The results revealed an ongoing increase in mid-span deflection without signs of stabilization over time. The recorded deflections for Bridges I and II reached 278 mm and 315 mm after nine years of service, respectively. As shown in Fig. 8, the measured deflection of the bridge significantly exceeds the design predictions based on various

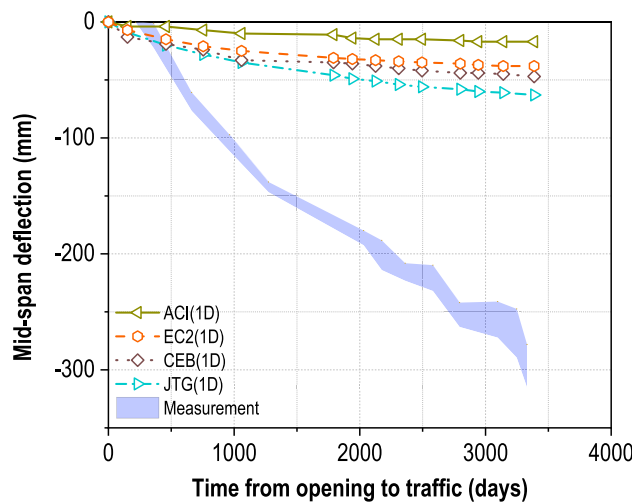


Fig. 8. Comparison of deflection development calculated with design code and the measured data for bridge I.

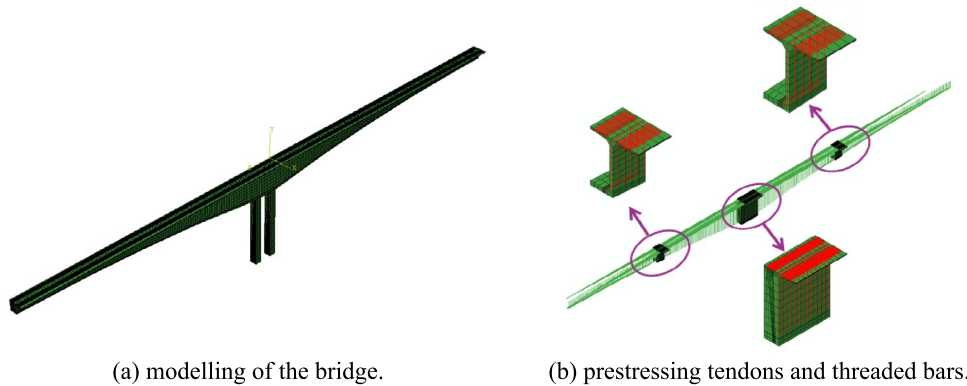


Fig. 9. FEM model of the bridge I (one-quarter of the structure).

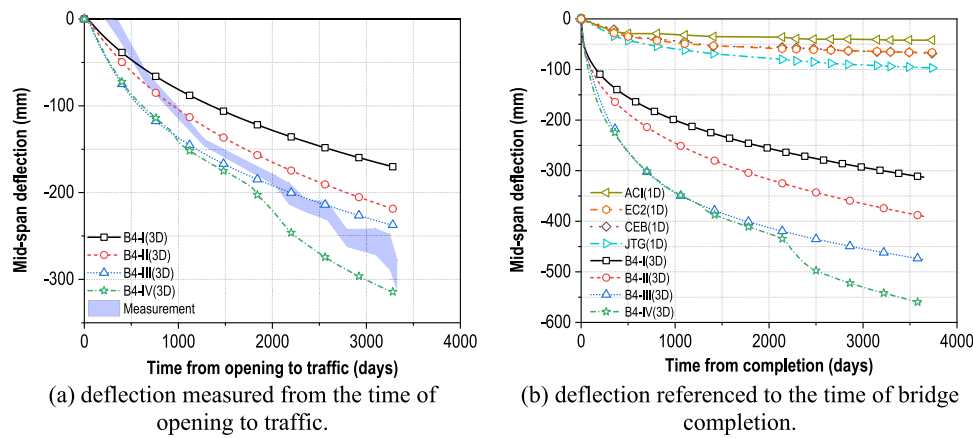
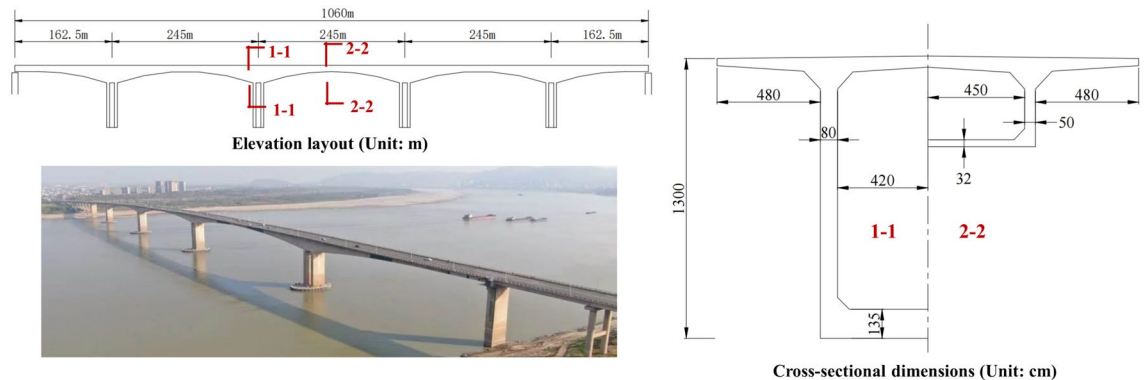
specifications. The deflection design derived from these specifications does not adequately reflect the actual deflection behaviour of the bridge.

Finite element modelling

To enhance computational efficiency, a three-dimensional finite element model representing one-quarter of the bridge is developed in Abaqus/Standard by exploiting structural symmetry, as shown in Fig. 9a. Segmental construction is simulated through sequential activation of initially deactivated components, following the actual construction schedule. This method enables accurate representation of staged loading effects on both the concrete and prestressing tendons.

Concrete components, including the box girder and piers, are modelled using C3D8 solid elements, while T3D2 truss elements are used for the prestressing tendons, which are assumed to be fully bonded to the surrounding concrete at their nodes. The concrete was modeled with 25,433 C3D8 elements and the tendons with 10,565 T3D2 elements. Given the uniform distribution and low volume ratio of steel reinforcement, rebars are smeared directly within the concrete and not modelled separately. As the tendons are nearly straight, only wobble friction is considered. The layout of tendons and reinforcement is presented in Fig. 9b. Prestressing is applied seven days after the casting of anchorage segments, with initial stress levels of 1300 MPa for tendons and 450 MPa for screw-threaded bars. Prestressing was applied seven days after the casting of the anchorage segments using initial stress levels of 1300 MPa for tendons and 450 MPa for screw-threaded bars, as specified in the design documents, with short-term losses such as friction and elastic shortening estimated at approximately 10% and calculated according to the method described in⁵². A linear-elastic constitutive model was adopted for the prestressed steel tendons since their expected stress levels under the investigated loading conditions remained within the elastic range.

The pier bases were modelled as rigid supports. At the closure segment of the side spans, the displacement in the y-direction was constrained, while at the closure segment of the midspan, symmetry boundary conditions were applied by restraining the z-direction displacement. Similarly, in the transverse direction of the bridge, symmetry boundary conditions were imposed by constraining the x-direction displacement.

**Fig. 10.** Comparison of long-term mid-span deflection for bridge I.**Fig. 11.** Elevation layout and cross-sectional dimensions of bridge II.

Results

A comparison of the long-term mid-span deflections obtained from numerical models and field measurements is presented in Fig. 10a. As the on-site monitoring of mid-span deflection commenced 180 days after the bridge was opened to traffic, the predicted deflection at that day is taken as the reference zero point.

It is evident that the deflection values predicted by all design codes are significantly lower than the measured values. Even the Chinese code JTG 3362, which provides the largest predicted deflection among the codes, underestimates the measured value by as much as 279%. In the conventional analysis (B4-I), although the predicted deflection increases after incorporating the B4 model, it still falls far short of the measured value. When the contribution of nonlinear creep is further considered in B4-II, the predicted deflection increases noticeably, yet it remains approximately 30% lower than the actual value. Building on this, B4-III additionally accounts for concrete cracking and the use of normal-strength reinforcing steel, while the relaxation of steel is still modelled based on code provisions. B4-III demonstrates high accuracy in the early stages of mid-span deflection prediction. However, the discrepancy increases over time. This growing error is primarily due to the insufficient consideration of relaxation in screw-thread within the design codes. By amplifying the relaxation screw-thread by an amplification factor of ten, B4-IV is able to realistically reproduce the mid-span deflection curve. The final mid-span deflection predicted by B4-IV reaches 314 mm, which closely matches the measured value. This highlights the necessity of considering enhanced relaxation effects of screw-thread, which lead to additional prestress losses and further reductions in structural stiffness.

To obtain the complete long-term deflection process of the Bridge I, the time of bridge completion is taken as the reference zero point, and the prediction results from each model are plotted, as shown in Fig. 10b. The mid-span deflection increases rapidly after the bridge is completed. By the time the field measurements begin, the predicted deflection from B4-IV has already reached 239 mm. Additionally, B4-III and B4-IV show nearly identical predictions in the early stages; however, after 2100 days, the amplified relaxation of the screw-thread causes the discrepancy between the two models to increase rapidly.

Bridge II: a five-span (162.5 + 3 × 245 + 162.5) PC bridge

Bridge details

Bridge II is a five-span prestressed concrete continuous rigid-frame bridge, with a span configuration of 162.5 m + 3 × 245.0 m + 162.5 m, as shown in Fig. 11. The superstructure is designed with a box girder cross-

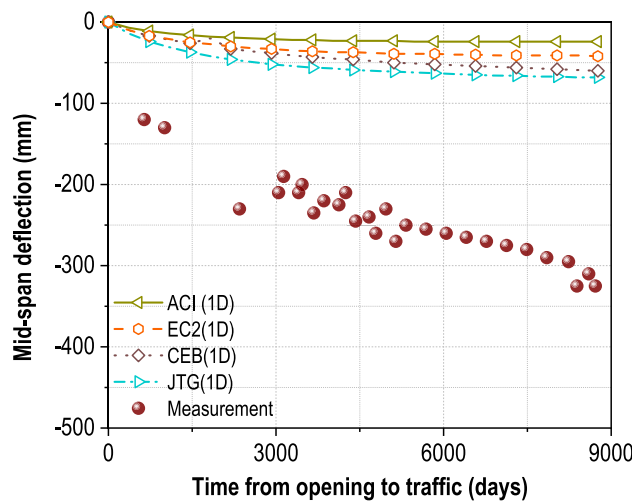


Fig. 12. Comparison of deflection development calculated with design code and the measured data for bridge II.

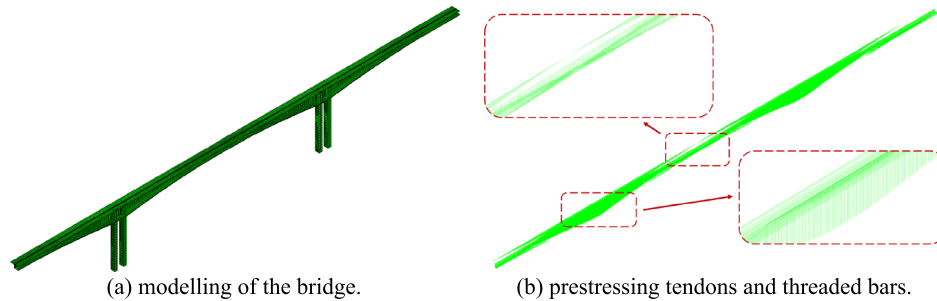


Fig. 13. FEM model of the bridge II (one-quarter of the structure).

section, where the top web width is set at 19.6 m and the bottom width is designed as 10 m, as detailed in Fig. 12. The box girder follows a quadratic parabolic profile, with the girder depth varying from 4.1 m at mid-span to 13 m at the piers. The bridge is constructed using the balanced cantilever method, where each of the four T-shaped frames is segmented into 32 pairs of cantilever segments. Longitudinal prestressing tendons in the top slab are arranged within the negative moment zones, with four tendons symmetrically anchored in each segment. Bottom slab tendons are placed in the positive moment regions to counteract tensile stresses. Transverse prestressing tendons are arranged in a staggered configuration along the longitudinal axis of the bridge, spaced at 50 cm intervals. Vertical prestressing screw-thread are embedded within the web of the box girder, also at 50 cm spacing, to enhance the shear resistance.

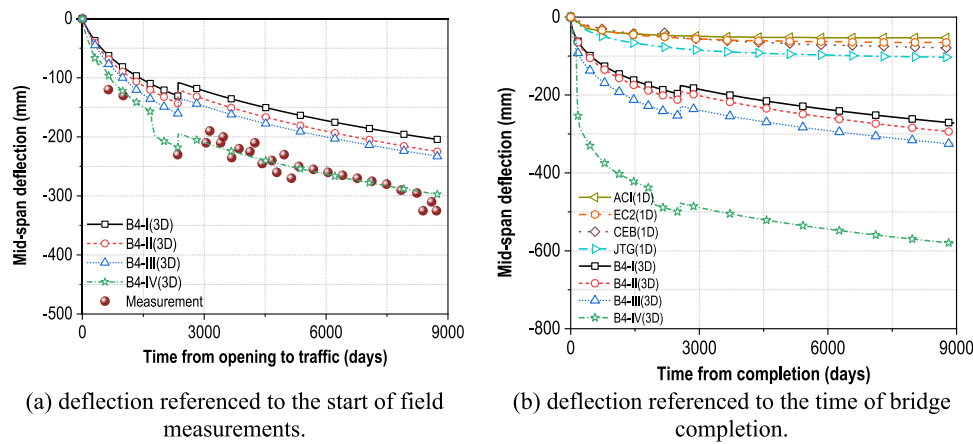
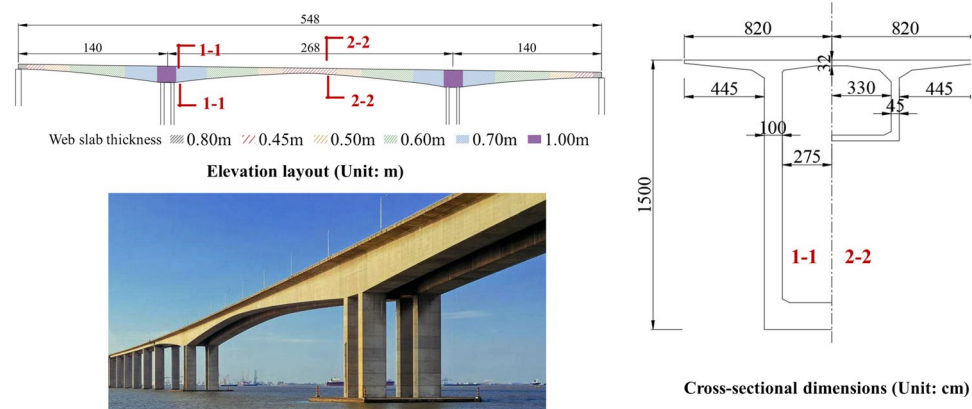
In Bridge II, deflection monitoring was initiated immediately after the bridge was opened to traffic. After 23 years of service, the recorded mid-span deflection reached 325 mm, as shown in Fig. 12. It can be observed that the deflection predictions based on the design code show significant discrepancies from the in-situ measurements.

Finite element modelling

A three-dimensional finite element model representing one-quarter of the bridge is developed in Abaqus/Standard, as shown in Fig. 13a. The cantilever construction process is simulated by sequentially activating girder segments according to the actual construction stages. Prestressing tendons are assumed to be fully bonded to the surrounding concrete, while conventional reinforcement is smeared into the concrete. The layout of prestressing tendons is illustrated in Fig. 13b, with initial stress levels of 1200 MPa for prestressing strands and 300 MPa for threaded bars. The same method as for Bridge I was used to determine the initial prestressing stress of Bridge II. The concrete consisted of 20,880 C3D8 elements and the tendons of 12,459 T3D2 elements.

Results

The long-term mid-span deflection results are illustrated in Fig. 14a. The deflection on the day the bridge was opened to traffic is defined as the reference zero point. All code-based predictions significantly underestimate the deflection, with the smallest deviation reaching 206%. The predicted deflection increases considerably with the incorporation of the B4 model (B4-I) and further inclusion of nonlinear creep effects (B4-II). For Bridge II,

**Fig. 14.** Comparison of the long-term mid-span deflection for bridge II.**Fig. 15.** Elevation layout and cross-sectional dimensions of bridge III.

the effects of concrete cracking, normal-strength reinforcement are relatively minor, resulting in only marginal improvement (B4-III). However, when the relaxation of screw-thread is amplified by a factor of ten in B4-IV, the predicted deflection curve aligns closely with the measured data. This confirms that vertical prestress loss plays a critical role in the long-term downward deflection observed in Bridge II. The complete long-term mid-span deflection process of the Bridge II is presented with the completion time as the reference zero point, as shown in Fig. 14b. Following the completion of the bridge, the mid-span deflection increases rapidly, with the deflection predicted by B4-IV reaching 275 mm by day 7350.

Bridge III: a three span (140 + 268 + 140) PC bridge

Bridge details

The Bridge III is a three-span prestressed concrete continuous rigid-frame bridge with spans of 140 m + 268 m + 140 m, as illustrated in Fig. 15. The most different between this case and other cases aforementioned is that there are several groups of cantilever downward-curved tendons anchored in the bottom of web. The superstructure adopts a box girder cross-section measuring 16.4 m in top slab width and 7.5 m at the bottom. The bridge is constructed using the balanced cantilever method, with the girder depth transitioning from 4.5 m at the mid-span to 15 m at the piers.

Longitudinal prestressing of the bottom slab at mid-span is achieved through 15 pairs of tendons, while the side spans are prestressed using 7 pairs of closure tendons. To mitigate the adverse effects of temperature variations, 4 pairs of closure tendons are installed in the top slab near the ends of the side spans. Additionally, transverse prestressing tendons are uniformly spaced at 50 cm intervals along the bridge. Each web contains two vertically arranged screw-threaded bars, also spaced longitudinally at 50 cm intervals. Given the critical role of vertical prestressing in enhancing the crack resistance of the structure, this case employs improved materials and refined tensioning techniques for the vertical elements. Furthermore, the web thickness is increased in the pier regions to enhance shear capacity. Conversely, it is reduced at the mid-span to improve material efficiency. The variation of web thickness is shown in Fig. 15. A secondary tensioning procedure is also implemented to compensate for potential prestress losses in the vertical direction. The procedure introduced an additional prestress equivalent to 5% of the design tensile control stress.

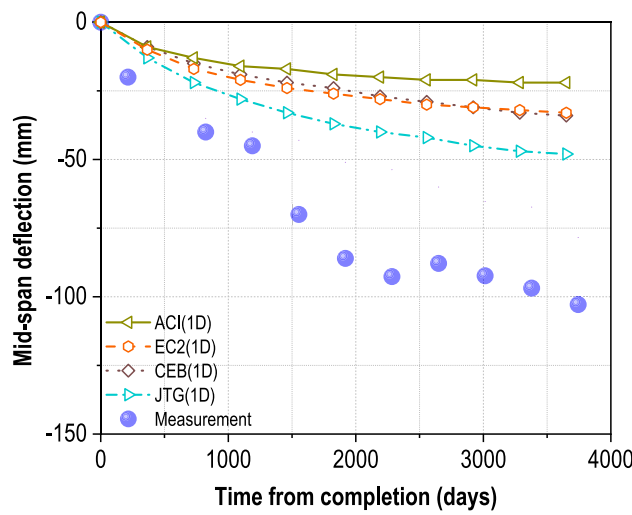


Fig. 16. Comparison of deflection development calculated with design code and the measured data for bridge III.

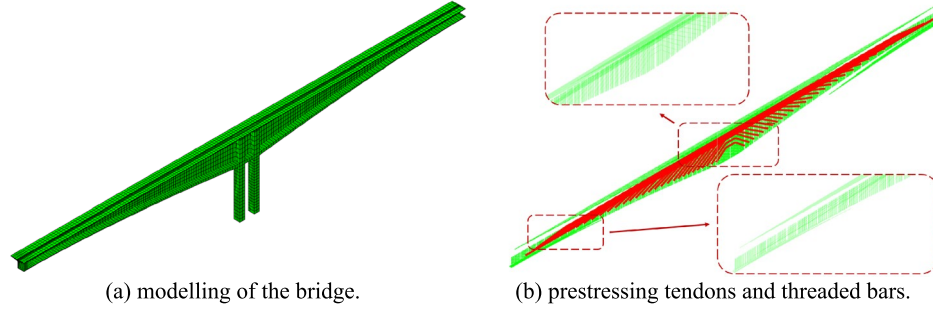


Fig. 17. FEM model of the bridge III (one-quarter of the structure).

Deflection monitoring of Bridge III commenced immediately upon its opening to traffic. After 10 years of service, mid-span deflections of 102.8 mm were recorded (Fig. 16). The deflection predicted in accordance with the design specifications approximates the measured values, though a slight discrepancy remains.

Finite element modelling

As with the previous cases, a three-dimensional finite element model representing one-quarter of the Bridge III is established in Abaqus/Standard, with the actual cantilever construction process simulated, as shown in Fig. 17a. The layout of the prestressing tendons is illustrated in Fig. 17b, with initial stress levels set at 1200 MPa for prestressing strands and 450 MPa for threaded bars. The approach used to define the initial stress was consistent with the one applied in Bridge I. The downward-curved tendons are highlighted with red. The concrete was represented by 19,438 C3D8 elements and the tendons by 9238 T3D2 elements. The modelling approaches for concrete creep, shrinkage, and prestress relaxation follow the same methodologies applied in the previous cases.

Results

Taking the deflection on the day of bridge completion as the reference zero point, the predicted mid-span deflection curves from design codes and numerical models are plotted and compared with field measurements, as shown in Fig. 18. Code-based predictions significantly underestimate the deflection. With the implementation of the B4 model (B4-I) and further consideration of nonlinear creep effects (B4-II), the predicted deflection already exceeds the measured value of Bridge I. After quantifying the contributions of concrete cracking, conventional-strength reinforcement, and screw-thread relaxation, the prediction from B4-III closely aligns with the measured deflection of Bridge II. Notably, B4-IV yields result nearly identical to B4-III, indicating that the relaxation of screw-thread has a negligible impact on the long-term deflection of bridge 3.

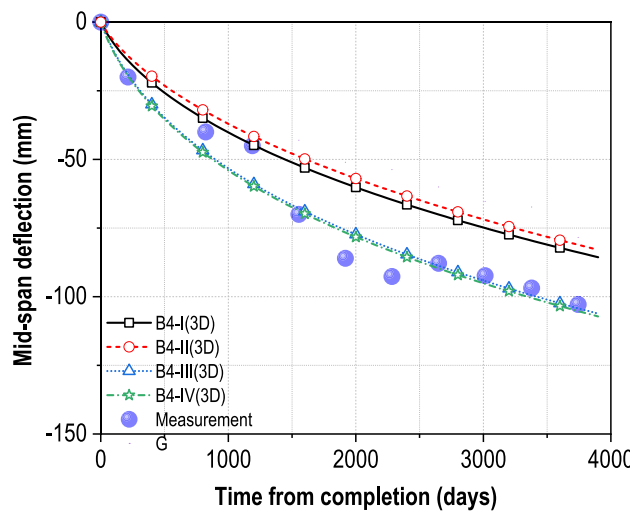


Fig. 18. Comparison of the long-term mid-span deflection for bridge III.

Section	Stress state under the combination of dead load and live load	Stress state under prestressing	Overall stress state	
Mid-span section				acceptable
				unacceptable
Near pier section (cantilever beginning section)				acceptable
				unacceptable

Table 5. Reasonable finished stress state of a three-span PC continuous bridge.

Discussions

Reasonable finished stress state and long-term deflection of PC bridges

The reasonable finished stress state of a long-span prestressed concrete continuous girder bridge refers to the initial stress state of the structure at the time of completion. It is the overall stress state of the structure after the prestress offsets the normal load combination (mainly the combination of dead load and live load). For instance, a three-span prestressed continuous bridge under external load combinations, the mid-span section exhibits a higher stress gradient at the upper fiber compared to the lower fiber, while sections near the piers show the opposite pattern with a greater stress gradient at the lower fiber. The prestressing design should generate a stress gradient that, when combined with the external load effects, maintains a consistent sign of stress gradients with the prestressing effects throughout the bridge, as shown in Table 5⁵³.

To investigate the long-term stress evolution in different bridge structural systems, a comparative analysis was conducted on the normal and shear stress variations of three bridges between their as-built condition and after years of service. The normal stress evaluation focused on three critical sections: the deck slab, web centreline, and bottom slab. For shear stress assessment, five representative locations were examined, comprising the deck slab, three longitudinal paths along the 1/4, 1/2 and 3/4 heights of the web, and the bottom slab. MATLAB smoothing technology is employed to reduce noise and enhance pattern visibility in stress distribution data along the longitudinal direction.

The normal stress evolution patterns of Bridge I under long-term service conditions are presented in Fig. 19. In the pier segments, compressive normal stresses in the top slab (7.7 MPa) calculate approximately 49.4% lower

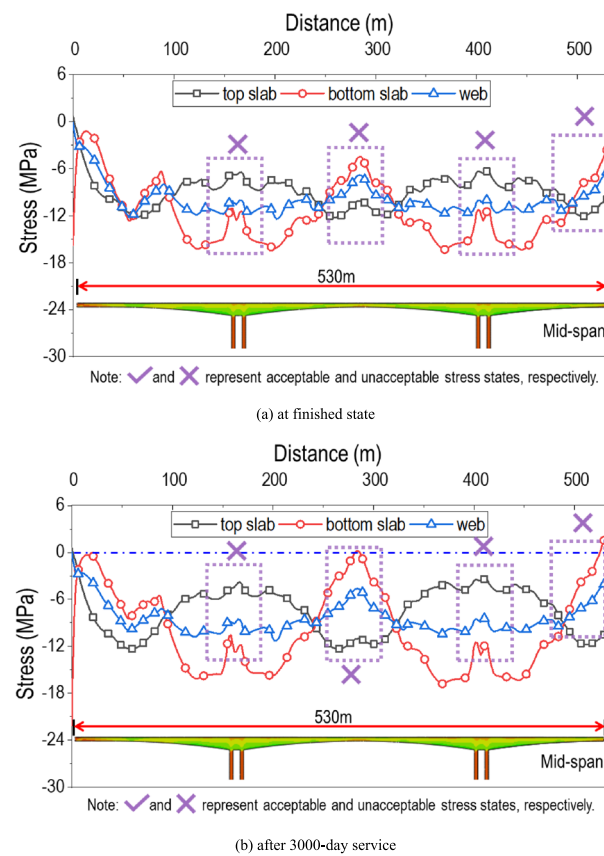


Fig. 19. Normal stress distribution distribution of bridge II.

than those in the bottom slab (15.14 MPa), with this differential stress distribution persisting in mid-span regions. These stress conditions are unfavourable for long-term deflection control. After 3000 service days, it shows the emergence of tensile stresses up to 0.2 MPa in the bottom slab of secondary and main spans, concurrent with a 24.8% reduction in compressive stress within the pier-supported top slab sections. This stress redistribution may potentially induce additional mid-span deflection at a rate of 13.61 mm/year.

Shear stress analysis reveals non-uniform distribution characteristics, with peak values concentrated in the central region of web (path 3). Over 3000 days of service, the shear stress along path 2 increased by approximately 1 MPa as shown in Fig. 20. The observed stress redistribution patterns show correlation with measured deflection trends, indicating progressive structural stiffness degradation.

The long-term normal stress evolution characteristics of Bridge III are systematically presented in Fig. 21. In the pier segments, the initial normal compressive stress in the top slab (approximately 18 MPa) is higher than that in the bottom slab (7.5 MPa), this is consistent with the reasonable stress state in Table 5. And after 3000 service days, the stresses in both the top and bottom slabs develop to around 10 MPa, the stress distribution is also beneficial for long-term deflection control. Consequently, the bridge exhibits a controlled mid-span deflection at an average rate of 8.8 mm/year, significantly lower than that observed in other case bridges.

Shear stress analysis indicates minimal variation across the structure Fig. 22, with no significant increases observed over the 3000-day monitoring period. Unlike other cases, the shear stress distribution remains stable, showing no pronounced concentration in critical regions. The uniform stress redistribution and reasonable stress state correlate with the reduced deflection rate, suggesting improved long-term performance compared to other case bridges.

Nonlinear creep effect

The nonlinear creep coefficient distribution development of the three case bridges was compared and analysed. Figure 23 shows the nonlinear coefficient distribution after 3000 days of service. The nonlinear creep effect of Bridge I is the largest, and the segment bottom plate area near the pier in the middle span is close to 1.8. Since the span is smaller than that of Bridge I, the nonlinear creep coefficient of Bridge II is about 1.2 in the segment area near the pier. Bridge III has no nonlinear creep effect, indicating that the compressive stress level of the entire bridge is less than 0.3.

The long-term structural behaviour was evaluated from the completion of bridge construction, defined as the time of closure and full application of second-stage dead loads. As shown in Fig. 24, the results reveal significant time-dependent effects of nonlinear creep on deflection development. The results from B4-II, which isolates

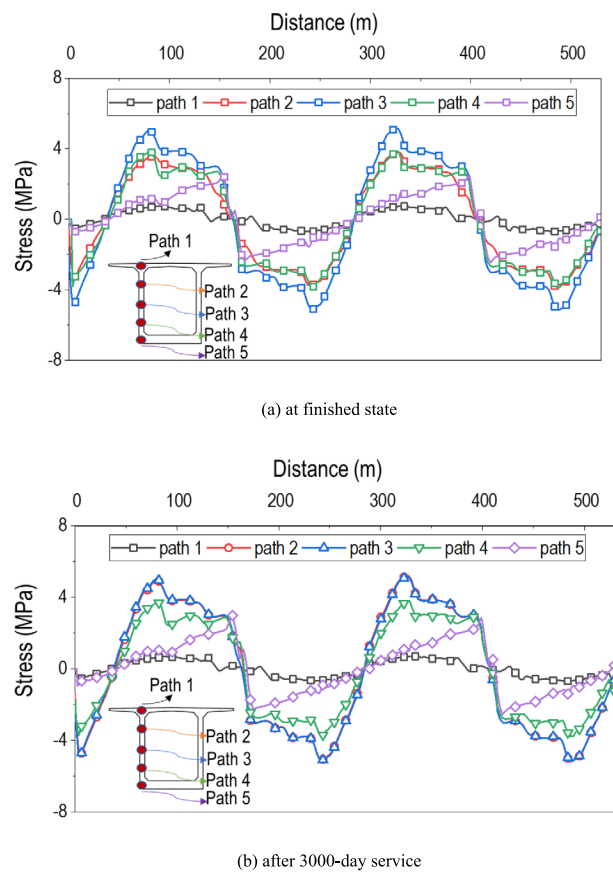


Fig. 20. Shear stress distribution of bridge II.

the nonlinear creep contribution by comparing with elastic deformation predictions with Eq. (24). The most pronounced nonlinear creep behaviour was observed in Bridge I among the cases studied, with creep-induced deflection components reaching a maximum of approximately 20% of the total displacement during service time. The nonlinear creep deflection ratios of the other two case bridges are less than 10%. The nonlinear creep deflection ratio is in agreement with the distribution presented in Fig. 23.

$$\delta = \left| \frac{\delta_{elas}}{\delta_{model}} - 1 \right| \quad (24)$$

where δ_{elas} is the deflection based on the elastic constitutive model B4-I; and δ_{model} is the deflection calculated by other models that consider additional factors as shown in Table 4.

The effects of nonlinear creep gradually stabilize as the structure continues to age. This stabilization occurs because the concrete material progressively approaches its final creep coefficient, while the sustained stresses that drive creep deformation reduce over time due to stress relaxation effects. The stabilized phase, typically reached after 5–10 years of service depending on environmental conditions and structural configuration, shows minimal additional creep-induced deflection, indicating that most of the time-dependent deformation has already occurred during the early service period.

Cracking effect

The crack pattern analysis of Bridge I reveals dominant failure mode characterized by flexural cracks concentrated near the bottom slab at mid-span locations. As shown in Fig. 25, the numerically simulated concrete damage distribution exhibits remarkable spatial consistency with observed crack patterns. The mid-span flexural cracks typically initiate at tensile stress concentration zones and propagate vertically. This strong correlation between simulated damage indices (0.65–0.87 in critical zones) and in-situ crack mapping validates the adopted damage mechanics approach, demonstrating its effectiveness in capturing stress-dependent crack evolution processes.

The deflection rate predicted by the B4-IV model shows a marked increase at approximately 2500 days of service (Fig. 10b). This change is attributed primarily to progressive mid-span crack development. The computational prediction is substantiated by field monitoring data, which demonstrate a 27% increase in the deflection rate ($\Delta\delta/\Delta t$) relative to initial service conditions. The correlation is observed between numerical modelling results and experimental measurements, indicating that structural stiffness degradation is significantly influenced by

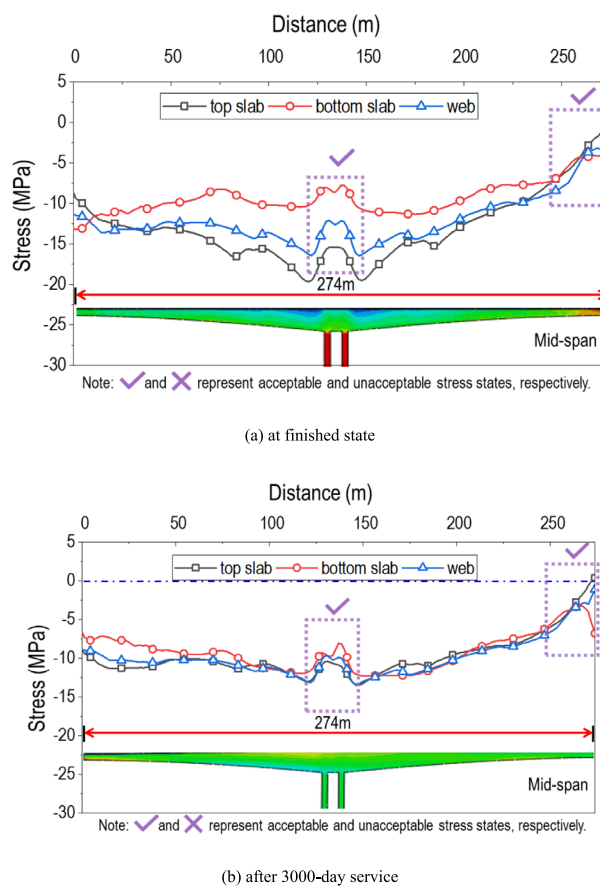


Fig. 21. Normal stress distribution of bridge III.

flexural crack propagation. This effect is found to be particularly pronounced in the mid-span region, where the maximum bending moment occurs under service loads.

The crack pattern analysis of Bridge II revealed two predominant failure mechanisms: (1) diagonal web cracks oriented at approximately 45° to the longitudinal axis, and (2) longitudinal splitting cracks in the top slab, with both crack types exhibiting maximum density between the quarter-span and mid-span regions. As illustrated in Fig. 26, the finite element-based damage simulation demonstrated strong congruence with experimental observations, particularly in terms of spatial distribution and crack propagation characteristics. The diagonal cracks consistently initiated in regions where the maximum principal tensile stress reached 2.2 to 3.5 MPa in critical elements, before propagating along compressive stress trajectories at angles ranging from 40 to 48 degrees relative to the horizontal plane. The comparison showed that the simulated damage indices correlated well with measured crack widths. This high-fidelity correspondence between numerical predictions and field measurements not only validates the implemented proposed model but also demonstrates its robust capability to simulate stress-governed fracture propagation in concrete bridge components under combined flexural-shear loading conditions. The onset of diagonal shear cracking triggers a nonlinear deflection response in Bridge II, manifested as a sudden slope change in the displacement curve (Fig. 14a) due to stiffness degradation in the web elements.

The cracking effect deflection ratio is shown in Fig. 27, it can be found that the values of Bridge I and Bridge II exhibit a gradual decreasing trend, reflecting the progressive enhancement of steel reinforcement effectiveness after cracking. Specifically, it declines from 0.41 to 0.23 between 500 and 3000d for Bridge I, while it experiences a 32% reduction over the same period for Bridge II. In contrast, Bridge III which sustains no visible cracking, experiences a linear 38.5% rise in value proportional to deflection.

Prestressing loss

From the FE analysis results of Bridge I, the mean prestress values of longitude tendons were computationally extracted for 31 cantilever tendon groups and one closure tendon group using a Python script. As illustrated in Fig. 28, after approximately 3,800 days of service for Bridge I, notable variations in calculated prestress losses are observed among different groups. The tendon stresses are distributed within a range of 965–1056 MPa, with individual variations observed among different groups of tendons. Specifically, a mean relaxation loss of approximately 15.5% is exhibited by Model B4-I, whereas slightly higher mean losses of 15.71% and 16.4% are shown by Models B4-II (incorporating nonlinear creep effects) and B4-III (considering cracking effects), respectively. The vertical prestress loss exhibits negligible influence on the longitudinal tendon prestress losses.

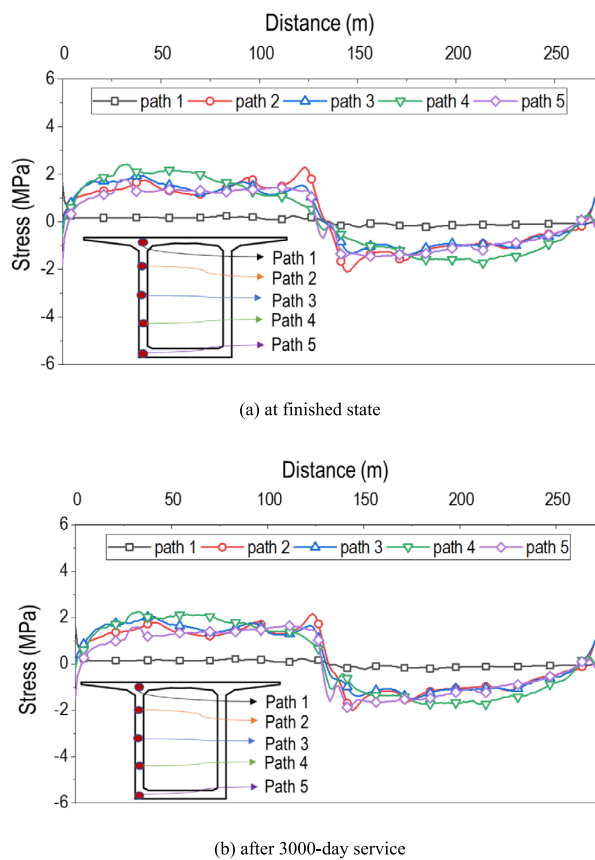


Fig. 22. Shear stress distribution of bridge III.

Computational results from model B4-IV indicate a relaxation loss of approximately 16.6% after 3,800 days of service. It is revealed by comparative analysis that concrete cracking has a more significant effect on prestress loss than nonlinear creep behaviour. This phenomenon can be attributed to stress redistribution resulting from crack formation, which subsequently amplifies tendon relaxation losses.

The influence of vertical prestressing loss on deflection ratios was analyzed across multiple case bridges as shown in Fig. 29. It was found that Bridge II was most significantly affected by vertical prestressing loss, with a maximum deflection ratio delta of approximately 0.7 being observed. A progressive variation in deflection ratio was observed over the service period, with Bridge III showing a consistently decreasing trend while Bridge I displayed initial reduction followed by subsequent increase. The minimum value of 0.32 was recorded for Bridge I at 2000 service days.

Tendon layout

The prestressing tendon layouts for Bridge II and Bridge III are detailed in Fig. 30. Bridge I and Bridge II were designed without downward-curved tendons, employing straight cantilever tendon configurations only, whereas Bridge III incorporates downward-curved tendons as part of its prestressing system. The lower maximum principal strain in Bridge III after 3000 days of service suggests better long-term performance compared to Bridge II, and this difference is crucial for assessing potential failure locations.

It is demonstrated through deflection analysis that the overall deflection is minimally affected even when substantial relaxation of vertical prestressing occurs in bridges where downward-curving tendons are implemented. Effective control of structural deflection is thereby confirmed to be provided by downward-curving tendons. Furthermore, different failure modes are identified through concrete crack pattern analysis: flexural cracking is observed at the mid-span of Bridge I, while shear cracking develops in the web of Bridge II. The shear-dominated crack pattern significantly alters strain distributions across the box section and triggers a sudden increase in vertical deflection (Fig. 14a). Following crack initiation, Bridge II exhibits a clear discontinuity in the deflection curve, with a noticeable inflection point appearing upon shear crack formation.

Conclusions

Based on the proposed multi-field time-dependent FE model, long-term behaviours of three record-span prestressed concrete are investigated. The main conclusions are summarized as:

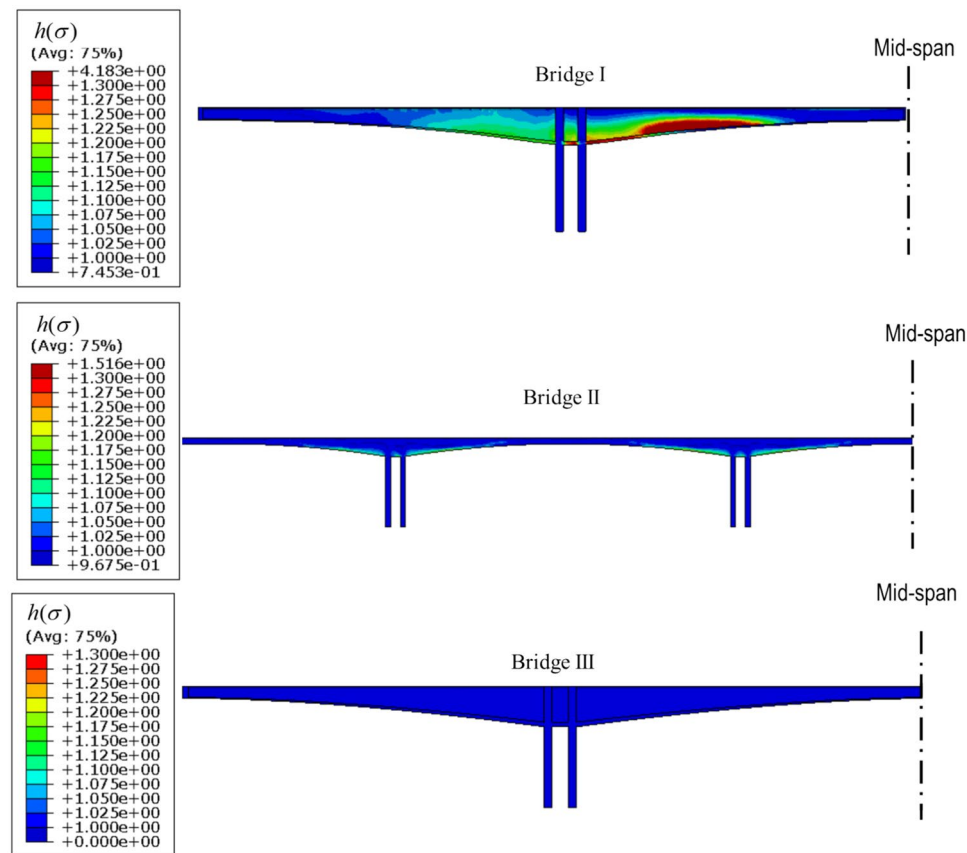


Fig. 23. Nonlinear creep coefficient distribution of case bridges based on the B4-IV model.

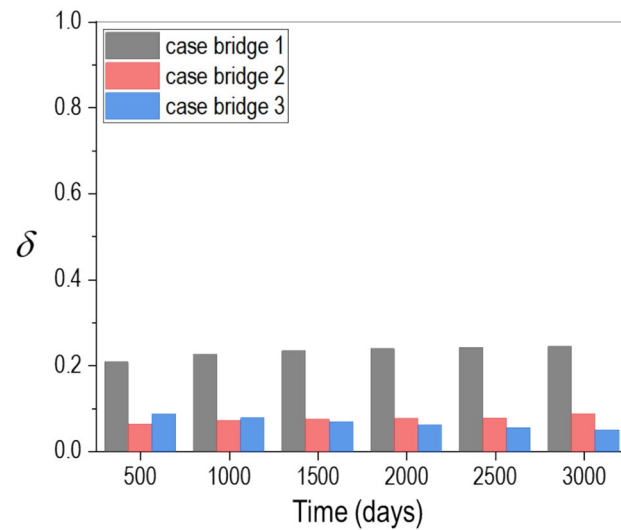
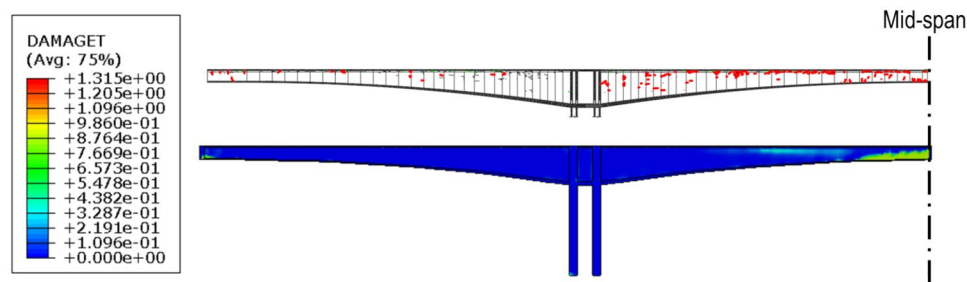
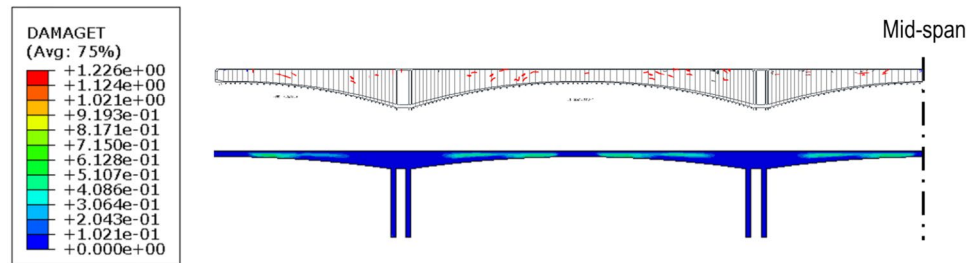


Fig. 24. Nonlinear creep deflection ratio of different case bridges.

- 1) Compared to the conventional FE model, the proposed multi-field time-dependent FE model additionally takes the nonlinear creep, concrete cracking and normal-strength rebars into account. Furthermore, the relaxation of the prestressing strands and screw-thread rebars is described in a more realistic way.
- 2) Long-term deflections of three record-span PC bridges are investigated. It seems the simulation results agree well with the in-site measurement. It is noteworthy to mention that all governing parameters are obtained from the mature models, i.e., B4 creep and shrinkage mode, CEB relaxation model, etc., without any artificial adjustment.

		3D FE model (<i>Abaqus/Standard</i>)				1D FE model (<i>Midas/Civil</i>)			
		B4-I	B4-II	B4-III	B4-IV	CEB	EC2	ACI	JTG
Concrete	Elastic	√	√			√	√	√	√
	CDP			√	√				
Creep	Linear	√				√	√	√	√
	Nonlinear		√	√	√				
Normal-strength rebar				√	√				
Relaxation for tendons		√	√	√	√	√	√	√	√
Relaxation for bars	Normal	√	√	√		√	√	√	√
	Amplified				√				

Table 4. Factors consider in different numerical models.**Fig. 25.** In-site inspection cracking and FEM results of bridge I.**Fig. 26.** In-site inspection cracking and FEM results of bridge II.

- 3) It is suggested that the design of the prestressing tendons should lead to the reasonable finished state of the bridge (Bridge III), which would inhibit the excessive deflection and cracking of PC bridges.
- 4) The relative thin thickness of the web slab of the box-section and straight layout of prestressing tendons are the mainstreaming practices, for PC bridges completed prior to the early 2000s (Bridge I and Bridge II). Consequently, the nonlinear creep effect and premature loss of vertical prestressing of screw-thread bars should be considered.
- 5) It is suggested that the layout of cantilever tendons should not be straight, but anchored in the blister/deviator at the bottom of the web slab. It would increase the compressive stress of the web slabs and diminish the risk of shear cracks resulting from the excessive prestressing loss of screw-thread bars.

PC girder bridges are always preferred by engineers as it is very competitive, both technically and economically. However, increasing the span capacity of PC girder bridges is controversial due to the anxiety about its long-term behaviour. This study for the first time systematically investigates the various long-term behaviours of three different record-span PC bridges. It is hopeful that the lessons from the three PC bridges would benefit the improvement of a PC bridge's long-term performance.

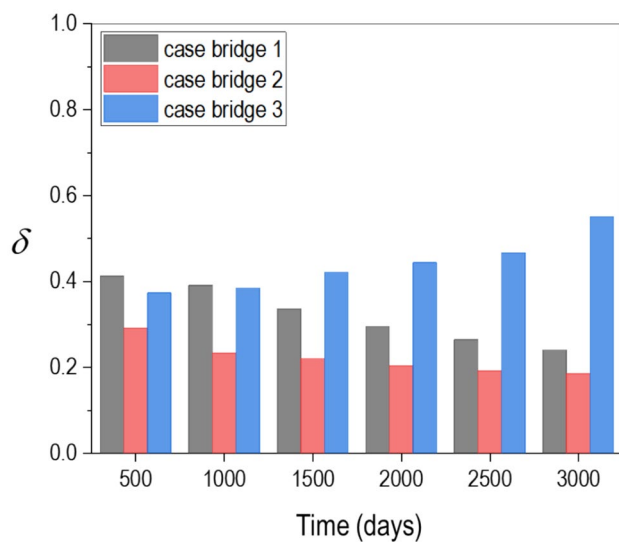


Fig. 27. Cracking effect deflection ratio of different case bridges.

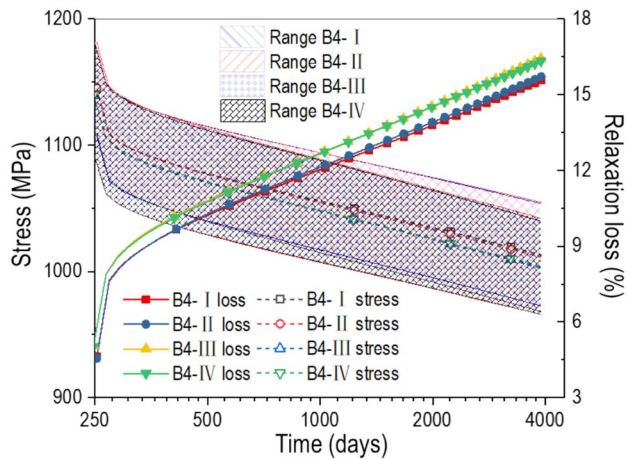


Fig. 28. Prestressing loss results of bridge I.

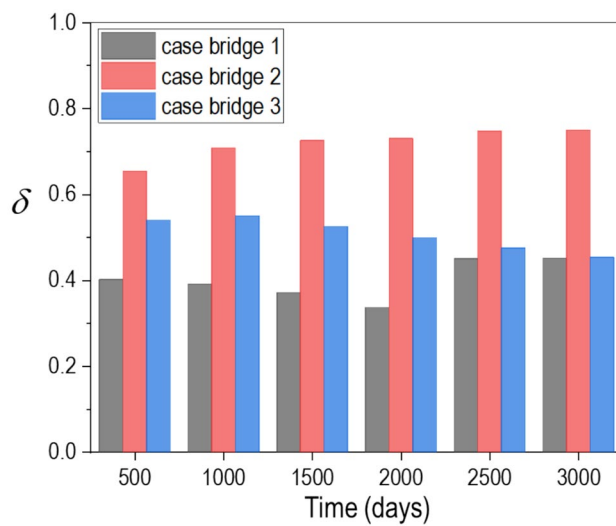
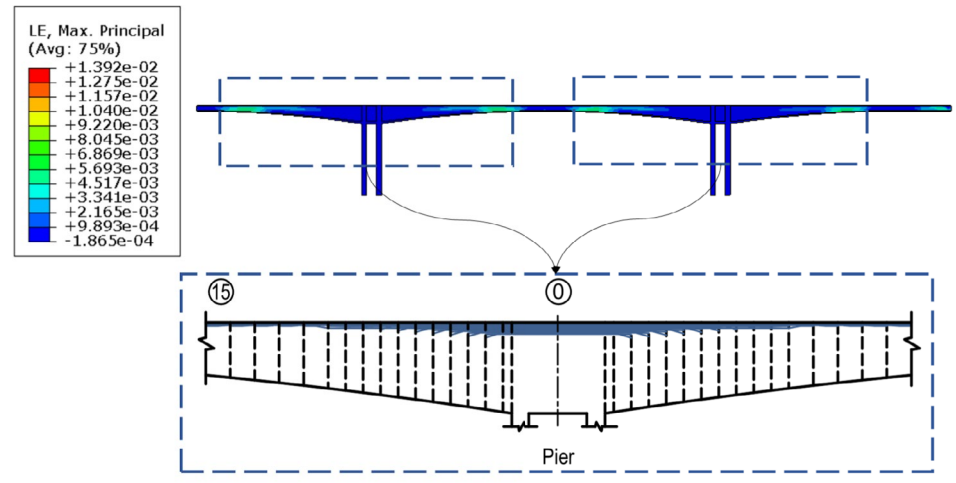
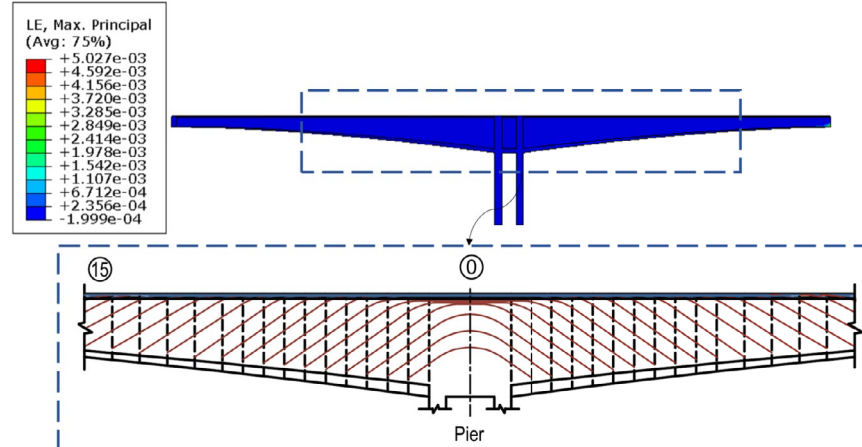


Fig. 29. Vertical prestressing loss deflection ratio of different case bridges.



(a) Bridge II.



(a) Bridge III.

Fig. 30. Longitude prestress tendons layout and concrete max principal strain at 3000-day.

Data availability

The data are presented in the manuscript. Furthermore, the detailed calculation process data are available from the corresponding author upon reasonable request.

Received: 17 August 2025; Accepted: 3 October 2025

Published online: 11 November 2025

References

- Huang, H., Huang, S.-S. & Pilakoutas, K. Modeling for assessment of long-term behavior of prestressed concrete box-girder bridges. *J. Bridge Eng.* **23**, 04018002. [https://doi.org/10.1061/\(ASCE\)BE.1943-5592.0001210](https://doi.org/10.1061/(ASCE)BE.1943-5592.0001210) (2018).
- Wang, Y., Zhu, J., Jia, S. & Akiyama, M. Time-dependent deflection prediction of long-span prestressed concrete bridges considering the environmental effects. *Eng. Struct.* **322**, 119163. <https://doi.org/10.1016/j.engstruct.2024.119163> (2025).
- Di Luzio, G., Cedolin, L. & Beltrami, C. Tridimensional long-term finite element analysis of reinforced concrete structures with rate-type creep approach. *Appl. Sci.* **10**, 4772. <https://doi.org/10.3390/app10144772> (2020).
- Bažant, Z. P., Hubler, M. H. & Yu, Q. Pervasiveness of excessive segmental bridge deflections: wake-up call for creep. *ACI Struct. J.* **108**, 766–774 (2011).
- Bažant, Z. P., Yu, Q. & Li, G.-H. Excessive long-time deflections of prestressed box girders. I: record-span bridge in palau and other paradigms. *J. Struct. Eng.* **138**, 676–686. [https://doi.org/10.1061/\(ASCE\)ST.1943-541X.0000487](https://doi.org/10.1061/(ASCE)ST.1943-541X.0000487) (2012).
- Bažant, Z. P., Yu, Q. & Li, G.-H. Excessive long-time deflections of prestressed box girders. II: numerical analysis and lessons learned. *J. Struct. Eng.* **138**, 687–696. [https://doi.org/10.1061/\(ASCE\)ST.1943-541X.0000375](https://doi.org/10.1061/(ASCE)ST.1943-541X.0000375) (2012).
- Raphael, W., Zgheib, E. & Chateauneuf, A. Experimental investigations and sensitivity analysis to explain the large creep of concrete deformations in the bridge of Chevrière. *Case Studies Constr. Mater.* **9**, e00176. <https://doi.org/10.1016/j.cscm.2018.e00176> (2018).
- Wang, W. & Gong, J. New relaxation function and age-adjusted effective modulus expressions for creep analysis of concrete structures. *Eng. Struct.* **188**, 1–10. <https://doi.org/10.1016/j.engstruct.2019.03.009> (2019).
- Bažant, Z. P. & Yu, Q. Relaxation of prestressing steel at varying strain and temperature: viscoplastic constitutive relation. *J. Eng. Mech.* **139**, 814–823. [https://doi.org/10.1061/\(ASCE\)EM.1943-7889.0000533](https://doi.org/10.1061/(ASCE)EM.1943-7889.0000533) (2013).
- Chhun, P., Sellier, A., LacARRIERE, L., Chataigner, S. & Gaillet, L. Incremental modeling of relaxation of prestressing wires under variable loading and temperature. *Constr. Build. Mater.* **163**, 337–342. <https://doi.org/10.1016/j.conbuildmat.2017.12.123> (2018).
- Lu, Z.-H., Wu, S.-Y., Tang, Z., Zhao, Y.-G. & Li, W. Effect of chloride-induced corrosion on the bond behaviors between steel strands and concrete. *Mater. Struct.* **54**, 129. <https://doi.org/10.1617/s11527-021-01724-8> (2021).
- Zhu, J., Meng, Q., Shi, T. & Yang, X. Long-term deformation analysis of prestressed concrete bridges under ambient thermal and vehicle loads. *Struct. Infrastruct. Eng.* **19**, 1656–1675. <https://doi.org/10.1080/15732479.2022.2052909> (2023).
- Birhane, F. N., Kim, S.-I. & Jang, S. Y. Long-term deflection of prestressed concrete bridge considering nonuniform shrinkage and crack propagation by equivalent load approach. *Appl. Sci.* **10**, 7754. <https://doi.org/10.3390/app10217754> (2020).
- Wu, S.-Y., Tong, T., Fang, Y. & Ge, F. Numerical model for time-dependent cracking and deflection of large-span concrete bridge structures. *Struct. Infrastruct. Eng.* <https://doi.org/10.1080/15732479.2024.2390465> (2024).
- Bažant, Z. P., Yu, Q., Li, G.-H., Klein, G. J. & Kríštek, V. Excessive deflections of record-span prestressed box girder. *ACI Concrete Int.* **32**, 44–52 (2010).
- Malerba, P. G. Bridge vulnerabilities and collapses: the Italian experience. *Struct. Infrastruct. Eng.* **20**, 976–1001. <https://doi.org/10.1080/15732479.2023.2277362> (2024).
- Deng, L., Wang, W. & Yu, Y. State-of-the-art review on the causes and mechanisms of bridge collapse. *J. Perform. Constr. Facil.* **30**, 04015005. [https://doi.org/10.1061/\(ASCE\)CF.1943-5509.0000731](https://doi.org/10.1061/(ASCE)CF.1943-5509.0000731) (2016).
- Jia, S., Han, B., Ji, W. & Xie, H. Bayesian inference for predicting the long-term deflection of prestressed concrete bridges by on-site measurements. *Constr. Build. Mater.* **320**, 126189. <https://doi.org/10.1016/j.conbuildmat.2021.126189> (2022).
- Ma, Y., Wang, L., Zhang, J., Xiang, Y. & Liu, Y. Bridge remaining strength prediction integrated with bayesian network and in situ load testing. *J. Bridge Eng.* **19**, 04014037. [https://doi.org/10.1061/\(ASCE\)BE.1943-5592.0000611](https://doi.org/10.1061/(ASCE)BE.1943-5592.0000611) (2014).
- Tong, T., Liu, Z., Zhang, J. & Yu, Q. Long-term performance of prestressed concrete bridges under the intertwined effects of concrete damage, static creep and traffic-induced cyclic creep. *Eng. Struct.* **127**, 510–524. <https://doi.org/10.1016/j.engstruct.2016.09.004> (2016).
- Li, S. W. et al. Three-dimensional nonlinear creep and shrinkage effects of a long-span prestressed concrete box girder bridge. *Struct. Concr.* **20**, 638–649. <https://doi.org/10.1002/suco.201800148> (2019).
- Meng, Q., Zhu, J. & Wang, T. Numerical prediction of long-term deformation for prestressed concrete bridges under random heavy traffic loads. *J. Bridge Eng.* **24**, 04019107. [https://doi.org/10.1061/\(ASCE\)BE.1943-5592.0001489](https://doi.org/10.1061/(ASCE)BE.1943-5592.0001489) (2019).
- Luis Francisco Rincón, Alvaro Viviescas, Edison Osorio, Carlos Alberto Riveros-Jerez, José Antonio Lozano-Galant, Long-term deformation assessment of a long-span concrete bridge built by the cantilever erection method, Latin American Journal of Solids and Structures (2022) 14.
- Han, X., Li, W. & Li, P. Long-term deflection analysis of large-span continuous prestressed concrete rigid-frame bridges based on a refined modeling approach. *Appl. Sci.* **13**, 9727. <https://doi.org/10.3390/app13179727> (2023).
- Qu, Z., Si, R., Jia, P. & Zhang, Y. Creep and relaxation responses of fly ash concrete: linear and nonlinear cases. *Case Stud. Constr. Mater.* **17**, e01562. <https://doi.org/10.1016/j.cscm.2022.e01562> (2022).
- Canestro, E., Strauss, A. & Sousa, H. Multiscale modelling of the long-term performance of prestressed concrete structures – Case studies on T-Girder beams. *Eng. Struct.* **231**, 111761. <https://doi.org/10.1016/j.engstruct.2020.111761> (2021).
- Chirdeep, N. R., Shivang, S. & Bahurudeen, A. Climate change impact on seismic vulnerability of aging highway bridges. *ASCE-ASME J. Risk Uncertainty Eng. Syst., Part A: Civil Eng.* **9**, 04023041. <https://doi.org/10.1061/AJRUAA.RUEENG-1068> (2023).
- Bažant, Z. P., Hauggaard, A. B. & Bewaa, S. Microprestress-solidification theory for concrete creep. II: algorithm and verification. *J. Eng. Mech.* **123**, 1195–1201. [https://doi.org/10.1061/\(ASCE\)0733-9399\(1997\)123:11\(1195\)](https://doi.org/10.1061/(ASCE)0733-9399(1997)123:11(1195)) (1997).
- Lubliner, J., Oliver, J., Oller, S. & Ofiate, E. A plastic-damage model for concrete. *Int. J. Solids Struct.* **25**, 299–326. [https://doi.org/10.1016/0020-7683\(89\)90050-4](https://doi.org/10.1016/0020-7683(89)90050-4) (1989).
- Cicekli, U., Voyiadjis, G. Z. & Al-Rub, R. K. A. A plasticity and anisotropic damage model for plain concrete. *Int. J. Plast.* **23**, 1874–1900. <https://doi.org/10.1016/j.ijplas.2007.03.006> (2007).
- Voyiadjis, G. Z., Taqieddin, Z. N. & Kattan, P. I. Anisotropic damage-plasticity model for concrete. *Int. J. Plast.* **24**, 1946–1965. <https://doi.org/10.1016/j.ijplas.2008.04.002> (2008).

35. Hillerborg, A., Modéer, M. & Petersson, P.-E. Analysis of crack formation and crack growth in concrete by means of fracture mechanics and finite elements. *Cem. Concr. Res.* **6**, 773–781. [https://doi.org/10.1016/0008-8846\(76\)90007-7](https://doi.org/10.1016/0008-8846(76)90007-7) (1976).
36. Bažant, Z. P. & Becq-Giraudon, E. Effects of size and slenderness on ductility of fracturing structures. *J. Eng. Mech.* **125**, 331–339. [https://doi.org/10.1061/\(ASCE\)0733-9399\(1999\)125:3\(331\)](https://doi.org/10.1061/(ASCE)0733-9399(1999)125:3(331)) (1999).
37. Lambert Li, X. X. Parametric study on numerical simulation of missile punching test using concrete damaged plasticity (CDP) model. *Int. J. Impact Eng.* **144**, 103652. <https://doi.org/10.1016/j.ijimpeng.2020.103652> (2020).
38. Hordijk, D. *Local approach to fracture of concrete* (Delft University of Technology, 1991).
39. Tong, T., Yuan, S. Q., Liu, Z. & Ruan, X. T. Three-dimensional finite element analyses for cyclic responses of precast segmental bridge piers accounting for bond-slip degradation. *Struct. Infrastruct. Eng.* **19**, 617–638. <https://doi.org/10.1080/15732479.2021.1961828> (2023).
40. R. Wendner, M.H. Hubler, Z.P. Bažant, 2013 The B4 model for multi-decade creep and shrinkage prediction, In: mechanics and physics of creep, shrinkage, and durability of concrete, American Society of Civil Engineers, Cambridge, Massachusetts, United States. <https://doi.org/10.1061/9780784413111.051>.
41. S. Wu, Z. Liu, T. Tong, Nonlinear creep analysis of long-span prestressed concrete bridges, in: 2024 (252–259). <https://www.scopus.com/inward/record.uri?eid=2-s2.0-85201539237&partnerID=40md5=eeb971ea9c1d8a7830025710d7772d5e>.
42. Bažant, Z. P. & Xi, Y. Continuous retardation spectrum for solidification theory of concrete creep. *J. Eng. Mech.* **121**, 281–288. [https://doi.org/10.1061/\(ASCE\)0733-9399\(1995\)121:2\(281\)](https://doi.org/10.1061/(ASCE)0733-9399(1995)121:2(281)) (1995).
43. Ohtani, Y. C. & Chen, W.-F. Hypoelastic-perfectly plastic model for concrete materials. *J. Eng. Mech.* **113**, 1840–1860. [https://doi.org/10.1061/\(ASCE\)0733-9399\(1987\)113:12\(1840\)](https://doi.org/10.1061/(ASCE)0733-9399(1987)113:12(1840)) (1987).
44. F.I. Du Béton, Model code 2010: final draft, International Federation for Structural Concrete, 2012.
45. Zhang, Y., Zhu, Y., Shao, X. & Li, B. Double-tensioned steel strands vertical prestress system on the webs of long-span PC Box-girder bridges. *J. Bridge Eng.* **26**, 05021005. [https://doi.org/10.1061/\(ASCE\)BE.1943-5592.0001715](https://doi.org/10.1061/(ASCE)BE.1943-5592.0001715) (2021).
46. C. Chen, Z. Kaiyin, W. Jian, Field measurement and analysis on the prestress loss of a long-span PC box Girder Bridge, In: 2011 International Conference on Electric Technology and Civil Engineering (ICETCE), IEEE, Lushan, China, 2011 (355–359). <https://doi.org/10.1109/ICETCE.2011.5776314>.
47. Nishio, H., Yagi, Y. & Ishikawa, Y. Prestressing analysis of large three-dimensional systems and prestress management. *ACI Struct. J.* **121**, 114–122. <https://doi.org/10.14359/51740857> (2024).
48. B. En, 1–1. Eurocode 2: Design of concrete structures—Part 1–1: General rules and rules for buildings, European Committee for Standardization (CEN) (2004).
49. ACI Committee, Building code requirements for structural concrete:(ACI 318–04); and commentary (ACI 318R-04), in: American Concrete Institute, 2004.
50. M. Ministry of Transport of the People's Republic of China, Code for design of highway reinforced concrete and prestressed concrete bridges and culverts, JTG D62–2004 (2004).
51. Shurbert-Hetzl, C., Daneshvar, D., Robisson, A. & Shafei, B. Data-enabled comparison of six prediction models for concrete shrinkage and creep. *Case Studies Construction Materials* **19**, e02406. <https://doi.org/10.1016/j.cscm.2023.e02406> (2023).
52. Kim, S.-H., Park, S. Y., Kim, S. T. & Jeon, S.-J. Analysis of short-term prestress losses in post-tensioned structures using smart strands. *Int. J. Concrete Structures Materials* **16**, 1. <https://doi.org/10.1186/s40069-021-00488-3> (2022).
53. Z. Liu, W. Dai, Z. He, L. Ji, Z. Li, J. Zhao, Design Method for Rational Completion Status of Long Span PC Girder Bridges, Bridge Construction (2010) 40–44.

Author contributions

The conceptualization, methodology, resources were provided by Tong T. and Liu Z. The finite element modelling and validation were performed by Wu S. Y. and Zhao C. Y. The writing was performed by Wu S. Y., Li J. T., and Tong T.. The reviewing and editing were by Tong T., Wu S. Y., and Li J. T.. Results were commented by Tong T..

Funding

Supported by the National Natural Science Foundation of China (52378134) and China Scholarship Council (202406090273).

Declarations

Competing interests

The authors declare no competing interests.

Additional information

Correspondence and requests for materials should be addressed to S.W.

Reprints and permissions information is available at www.nature.com/reprints.

Publisher's note Springer Nature remains neutral with regard to jurisdictional claims in published maps and institutional affiliations.

Open Access This article is licensed under a Creative Commons Attribution-NonCommercial-NoDerivatives 4.0 International License, which permits any non-commercial use, sharing, distribution and reproduction in any medium or format, as long as you give appropriate credit to the original author(s) and the source, provide a link to the Creative Commons licence, and indicate if you modified the licensed material. You do not have permission under this licence to share adapted material derived from this article or parts of it. The images or other third party material in this article are included in the article's Creative Commons licence, unless indicated otherwise in a credit line to the material. If material is not included in the article's Creative Commons licence and your intended use is not permitted by statutory regulation or exceeds the permitted use, you will need to obtain permission directly from the copyright holder. To view a copy of this licence, visit <http://creativecommons.org/licenses/by-nc-nd/4.0/>.

© The Author(s) 2025